


Research Article

Experimental Investigation on the Initiation of Hydraulic Fractures from a Simulated Wellbore in Laminated Shale

Yang Liu,^{1,2} Congrui Chen,¹ Tianshou Ma ,^{2,3} Gongsheng Zhu,² Nian Peng,² and Xi Zhang⁴

¹School of Mechatronic Engineering, Southwest Petroleum University, Chengdu, Sichuan 610500, China

²State Key Laboratory of Oil & Gas Reservoir Geology and Exploitation, Southwest Petroleum University, Chengdu, Sichuan 610500, China

³State Key Laboratory of Geomechanics and Geotechnical Engineering, Institute of Rock and Soil Mechanics, Chinese Academy of Sciences, Wuhan, Hubei 430071, China

⁴SCT Operations Pty Ltd, Wollongong, NSW 2500, Australia

Correspondence should be addressed to Tianshou Ma; matianshou@126.com

Received 15 June 2021; Accepted 13 October 2021; Published 2 November 2021

Academic Editor: Hao Xiong

Copyright © 2021 Yang Liu et al. Exclusive Licensee GeoScienceWorld. Distributed under a Creative Commons Attribution License (CC BY 4.0).

Understanding the formation mechanisms of complex fracture networks is vitally important for hydraulic fracturing operations in shale formation. For this purpose, a hydraulic fracturing experiment under a core-plunger scale is conducted to investigate the impact of the bedding plane angle, borehole size, and injection rate on fracture initiation behaviors of laminated shale rock. The results on rock properties demonstrate that the anisotropic characteristics of shale rock are reflected not only in elastic modulus but also in tensile strength. The results of fracturing experiments show that the bedding plane dip angle and borehole size have significant effects on fracture initiation behaviors, in that fracture initiation pressure (FIP) decreases with the increase of those two factors. The impact of injection rate, by contrast, has no obvious variety regulation. The above data is further used to validate our previously proposed fully anisotropic FIP model, which shows better agreement with experimental results than those using other models under various parameter combinations. Finally, a postfracturing analysis is performed to identify the fracture growth patterns and the microstructures on the fracture surfaces. The results show that the hydraulic fractures (HFs) always grow along mechanically favorable directions, and the potential interaction between HFs and bedding planes mainly manifests as fracture arrest. Meanwhile, the roughness of fracture surfaces is physically different from each other, which in turn results in the difficulties of fluid flow and proppant migration. The findings of this study can help for a better understanding of the fracture initiation behavior of laminated shale rock and the corresponding fracture morphology.

1. Introduction

Horizontal drilling in combination with hydraulic fracturing is now an efficient method for extracting oil and gas from unconventional reservoirs due to its ultralow permeability. Taking shale reservoirs as an example, large engineering practices have proved that the complexity of 3D fracture networks (FNs) after fracturing plays a decisive role in ensuring initial productivity and improving ultimate recovery. This implies that understanding the formation mechanisms of FNs is vitally important for hydraulic fracturing treatment design and operation.

The formation process of FNs necessarily includes initiation, propagation, and termination [1]. The pressure responses and fracture trace angle at the initiation stage are generally taken as the tool linking lab-scale fracturing with field-scale application [2, 3] and forecasting the conditions of initiating multiple HFs from a horizontal well [4]. In terms of shale formations, the well-developed bedding planes, faults, natural fractures (NFs), and foliation planes could lead to more complex fracture growth patterns because the HFs emanating from the wellbore or perforations may frequently interact with them [5]. Beugelsdijk et al. [6], Zhou and Xue [7], and Abass and Lamei [8] artificially introduced some NFs in cement blockfor

HF to encounter by means of heating and air cooling treatment and investigated the influence of NF conductivity, stress regimes, and injection rate on fracture growth behaviors. Zhou et al. [9], Gu et al. [10], and Chuprakov et al. [11] experimentally investigated the activation mechanisms that a fluid-driven HF approaches to NFs. Results reveal four typical interaction scenarios when HF encounters NFs, i.e., HF penetrating through NF plane, HF arrested by NF plane, HF deflecting along NF plane, and fracture offset. Athavale and Miskimins [12] examined the nature of HF interaction with NF using laminated specimens, where the bonded interface between layers was considered the filled NF. Olson et al. [13] embedded a thin glass plate into cast hydrostone to act as the cemented NFs and found that the oblique embedded NFs prefer to deflect the fluid-driven HFs comparing with NFs orthogonal to the created fracture trajectory. Similar phenomena were also observed by Fan and Zhang [14]. Lin et al. [15] conducted fracturing experiment for Longmaxi shale under the core-plunger scale to study the impacts of rock anisotropy on breakdown pressure and fracture width evolution. Besides, acoustic emission (AE) monitoring and computerized tomography scanning techniques were introduced to study the pressure responses and dynamic growth process of NFs during fracturing [16–18]. Results showed that shear events were detected in the vicinity of weak bedding planes around the wellbore prior to HF initiation.

Analytical and numerical solutions were also the commonly used ways to investigate the near-wellbore fracture initiation and propagation behaviors. Recent studies have shown that all laminated shale rocks display an obvious anisotropy in mechanical properties, including elastic modulus, Poisson's ratio, tensile strength, and fracture toughness ([19–21]. On account of this, two alternative solutions, namely, the anisotropic tensile-strength-based (ATSB) model [22, 23] and the fracture-mechanics-based (FMB) model [24], were recommended to illustrate the fracture initiation features from the wellbore wall. On the other hand, Zhang et al. [25, 26], Lecampion et al. [27], and Chen et al. [28] numerically simulated the effect of geologic discontinuities on the growth of fluid-driven HF. Results indicated that the failure behaviors of NFs when HF approaches largely depend on the stress distribution at the HF tip and the properties of NFs. Besides, for the case where wellbore contains both NFs and HFs, Liu et al. [29] studied the near-wellbore fracture propagation behaviors under various parameter combinations. Results, depending on which fracture grows, revealed four typical fracture growth geometries.

The primary concern of previous studies is the impact of rock anisotropies on the growth of HFs and interactions between the HFs and NFs or bedding planes. However, the formation mechanisms and regulation strategies of NFs were not entirely known, and the morphology of fracture surfaces is almost completely neglected. In fact, the complex fracture distribution and the characteristics of fractured surfaces play a decisive role in the transport and settling of lost circulation materials and proppant [30, 31]. More importantly, the connections between the fracturing experiments and the relevant theoretical models have not been established. On account of this, we performed core-plunger scale hydraulic

fracturing experiment to investigate the fracture initiation behaviors of laminated shale rock.

This paper is organized as follows. In Section 2, rock specimens with various bedding dip angles were prepared from the same shale outcrop. A scheme of orthogonal tests which included three factors and three levels was designed to study the combined impact of bedding dip angle, borehole size, and injection rate. We next presented the experiment results and gave an adequate explanation for the observed experimental phenomena. The anisotropic characteristics of shale rock in elastic modulus, Poisson's ratio, tensile strength, and fracture toughness were fully revealed through fundamental rock mechanics experiments. The general features of the fracturing experiment were analyzed. The peak injection pressure or FIP data was adopted for validating the proposed FIP model. The effects of the abovementioned factors on FIP were also discussed. Finally, a postfracturing analysis was performed for the fracture propagation patterns, so as to identify the micromorphologies on the fracture surfaces.

2. Experimental Methodology

2.1. Sample Preparation. Test materials used in this paper were collected from the Silurian shale outcrops of the Longmaxi formation in Changning County, Sichuan Province, China. The Longmaxi shale displays a dull black color and clear bedding planes, and it primarily consists of quartz, clay minerals, dolomite, feldspar, and pyrite, with the relative content of 51.05%, 17.76%, 14.06%, 13.54%, 1.97%, and 1.63%, respectively. To minimize the error resulting from the sample difference, shale blocks with a size of 500 mm × 400 mm × 300 mm were selected to ensure that shale specimens used for all kinds of tests at a given bedding dip angle were taken from the same core column. This approach offers the benefit of correlating the rock mechanics testing results with the experimental fracture initiation pressures and improving the comparability of data. The bedding dip angle (β) was defined as the angle between the sample axis and the normal direction of the bedding plane.

Three different bedding plane dip angles, i.e., 0°, 45°, and 90°, were selected to characterize the anisotropic properties of shale, as shown in Figure 1(a). Uniaxial compressive strength (UCS), elastic modulus, and Poisson's ratio were measured on a cylindrical rock sample with a nominal size of $\Phi 25$ mm × 50 mm. Tensile strength was measured on a Brazilian disc with a nominal diameter of 50 mm and a nominal thickness of 25 mm, as shown in Figure 1(b). The cracked chevron notched Brazilian disc (CCNBD) specimen was used to measure fracture toughness, where the geometry and nominal size of the CCNBD specimen were displayed in Figure 1(c). The core-plunger scale hydraulic fracturing experiments were conducted on a nonstandard cylindrical rock sample, where a centered hole with a nominal depth of 60 mm was drilled from the top of the cylinder to simulate the actual borehole, as illustrated in Figure 1(d). Each centered hole was drilled by using a new micro drill bit to avoid boundary effect induced by bit wear. In addition, the upper and lower surfaces of all cored samples were ground to

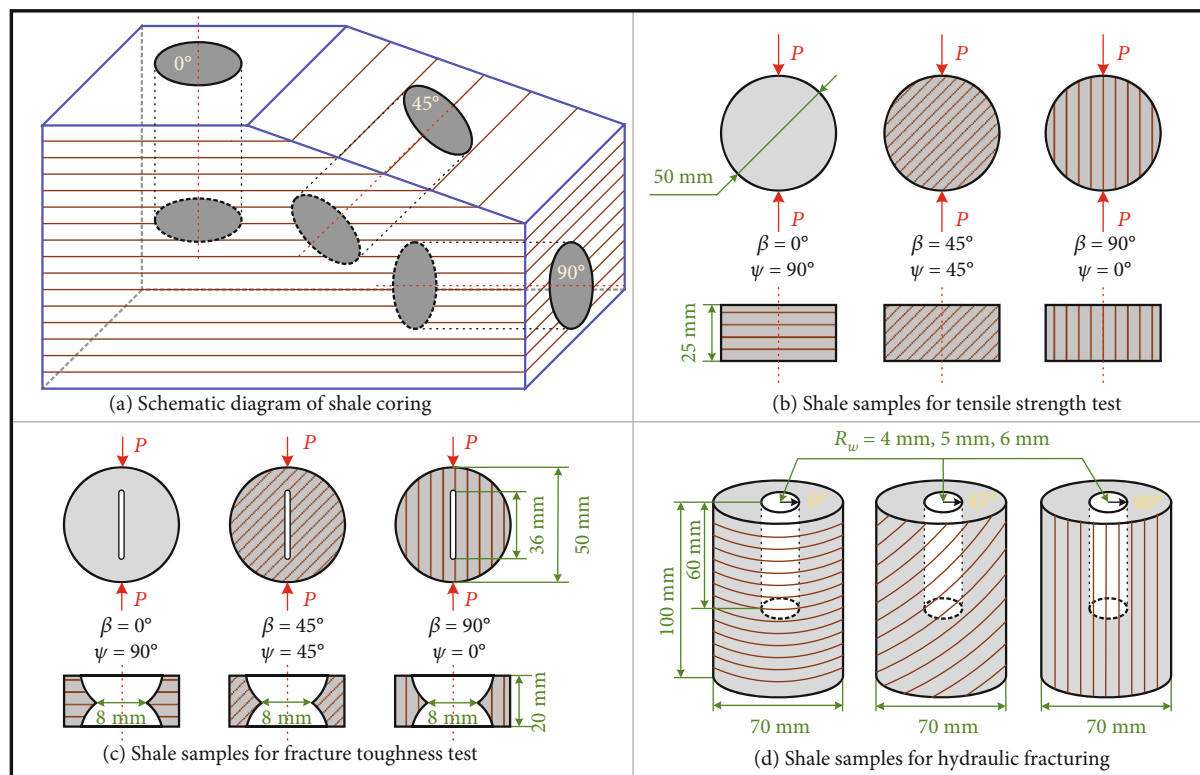


FIGURE 1: Preparation of shale samples with different bedding angles used for (a) tensile strength test (b), fracture toughness test (c), and core-scale hydraulic fracturing test (d).

obtain smooth parallel surfaces using a face grinder to make force deployed evenly on the specimen.

2.2. Experimental Apparatus. The core-scale fracturing experiments were conducted by using a self-designed triaxial multifield coupling testing system, as shown in Figure 2(a). The testing system is mainly composed of a servohydraulic station, a triaxial pressure chamber, a loading rack, a confining pressure supercharger (CPS), a pore pressure supercharger (PPS), and measurement and control system. The triaxial pressure chamber covering the testing cell around the specimen applies isostatic confining pressure on the sample by compressing confining fluid. The specimen can be heated indirectly by the thermal fluids within the pressure chamber. The maximum injection pressure and the maximum confining pressure of the testing system could reach 80.0 MPa.

The sample was connected to the top and bottom squeeze heads by a rubber sleeve, as illustrated in Figure 2(b). O-ring was installed on the top squeeze head to prevent pressure communication between the borehole and the pressure chamber, as shown in Figure 2(c). Fluid was injected into the sample through the top squeeze head at a given injection rate. The injection rate was measured by the displacement control mode, and thus, the injection rate can be estimated by the product of displacement per unit time and the cross-sectional area of the piston. The diameter gages installed on the middle position of the specimen, as

shown in Figure 2(b), were employed to monitor the evolution of specimen circumference. During the hydraulic fracturing experiment, all the experimental data, including axial stress, confining pressure, injection pressure, and radial deformation, were gathered with a frequency of 1 Hz.

2.3. Experimental Scheme. The axial stress imposed on the surface of the top squeeze head was set as 25.0 MPa to get a good seal and prevent injected fluids from leaking from the borehole. The confining pressure was actually negligible for all of the hydraulic fracturing tests. All experiments were conducted at the temperature of 20.0°C, which can be controlled by the thermal fluids within the pressure chamber. Data monitoring found that thermal fluids could bring about approximately 0.24 MPa confining pressure. Thus, the confining pressure is specified as 0.24 MPa for subsequent analysis.

For core-scale hydraulic fracturing tests, the bedding dip angle, borehole size, and injection rate may have various degrees of effects on FIP and fracture growth patterns. For this purpose, an orthogonal consideration with three-factor and three-level choices was adopted to study the interplay of these factors, as shown in Table 1. Three different borehole sizes were selected to analyze its influence on FIP, in which the experimental studies on the core-scale hydraulic fracturing behavior of various rocks provide a reference for this parameter value [15, 32]. The injection rates were chosen referring to the previous studies that used similarly sized specimens [8, 33].

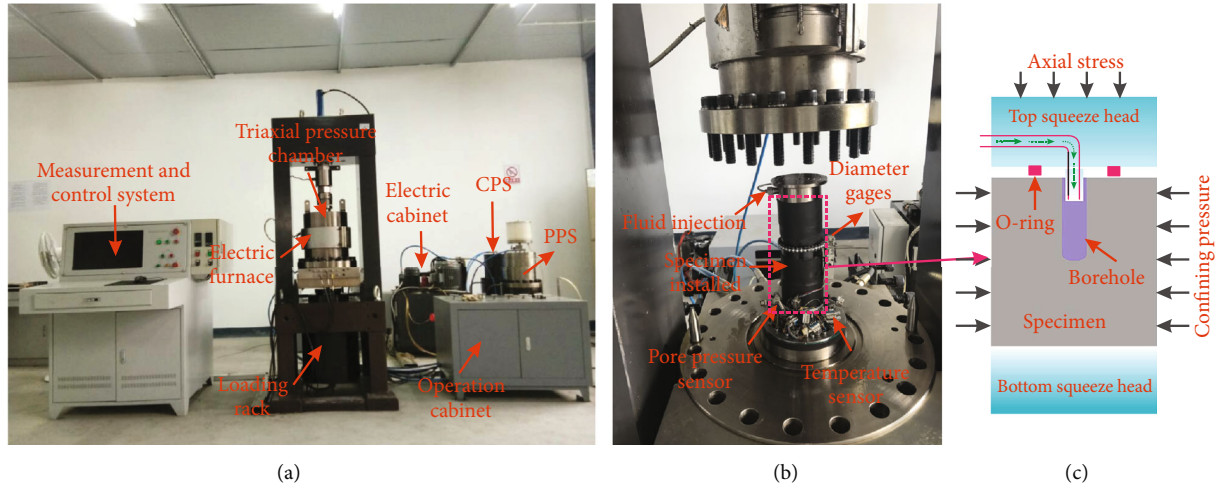


FIGURE 2: Photograph of experimental devices: (a) core-scale hydraulic fracturing testing system; (b) details of specimen installed; (c) details around the specimen.

TABLE 1: The three-factor and three-level orthogonal experimental design.

No.	β ($^{\circ}$)	R_w (mm)	q (mL/s)
HF-1	0	4	0.75
HF-2	0	5	0.35
HF-3	0	6	0.15
HF-4	45	4	0.35
HF-5	45	5	0.15
HF-6	45	6	0.75
HF-7	90	4	0.15
HF-8	90	5	0.75
HF-9	90	6	0.35

3. Results and Analysis

3.1. Anisotropic Characteristics of Shale Rock. Figure 3 shows the testing results of partial rock mechanics parameters of shale rock under various bedding dip angles. The experiment needs to be stressed that the experiment numbers of each type of test are corresponding to each other and the required specimens are taken from the same core column (e.g., specimens used for EM-1, PR-1, BTS-1, KIC-1, and HF-1 tests are obtained from a longer core column). It is clearly observed that the elastic modulus and tensile strength could be significantly impacted by the bedding dip angle, and these two parameters generally decrease with the increasing of the bedding dip angle. This illustrates that shale rock exhibits strong elastic and strength (compressive and tensile strength) anisotropy. Since the UCS is beyond the scope of this study, it will not be covered in as much detail as other parameters. By contrast, the changes in Poisson's ratio and fracture toughness are not apparent with the bedding dip angle. These results are consistent with the tests conducted by Sayers [21] and Jin et al. [34], which confirms that the anisotropic degree of elastic modulus and tensile

strength in shale rock is stronger than Poisson's ratio and fracture toughness.

3.2. General Features of the Hydraulic Fracturing Experiments.

According to the above experimental scheme, the evolution of injection pressure and radial displacement with respect to the injection time during hydraulic fracturing are displayed in Figure 4. Since the fracturing fluid injecting the borehole is progressive, the injection pressure and the radial displacement will have no significant change until the borehole is filled with fluid. Thus, partial data in this stage are removed from the figure.

From Figure 4(a), we can find out that the injection pressure increases dramatically during the fracturing stage and the pressurized rate is directly proportional to the injection rate. Generally, fracture initiation takes place at the first inflection point where the injection pressure curve deviates from linearity before formation breakdown. In other words, the FIP is less than or equal to the peak injection pressure (also known as formation breakdown pressure). However, for the present experiment, there is no obvious initiation point observed in the pump pressure curve; thus, the peak injection pressure is defined as FIP in this paper. Obviously, the FIP shows significant differentiation for these nine group experiments. This phenomenon may be driven in large part by tensile strength anisotropy, and other factors of course play a part, which will be analyzed in the following section. The peak is followed by a sudden drop in the injection pressure. This is because the created fracture propagates immediately to the outer surface of the specimen, which could result in pressure communication between borehole and pressure chamber.

From Figure 4(b), we can observe that the radial displacement increases sharply and gets the maximum immediately after the injection pressure reaches FIP. Simplistically, half of the maximum circumferences can be roughly treated as the width of hydraulic fracture [35]. The fracture widths thus determined are, respectively, 0.668 mm, 0.551 mm, 0.114 mm, 0.131 mm, 0.187 mm, 0.094 mm, 0.122 mm, 0.121 mm, and

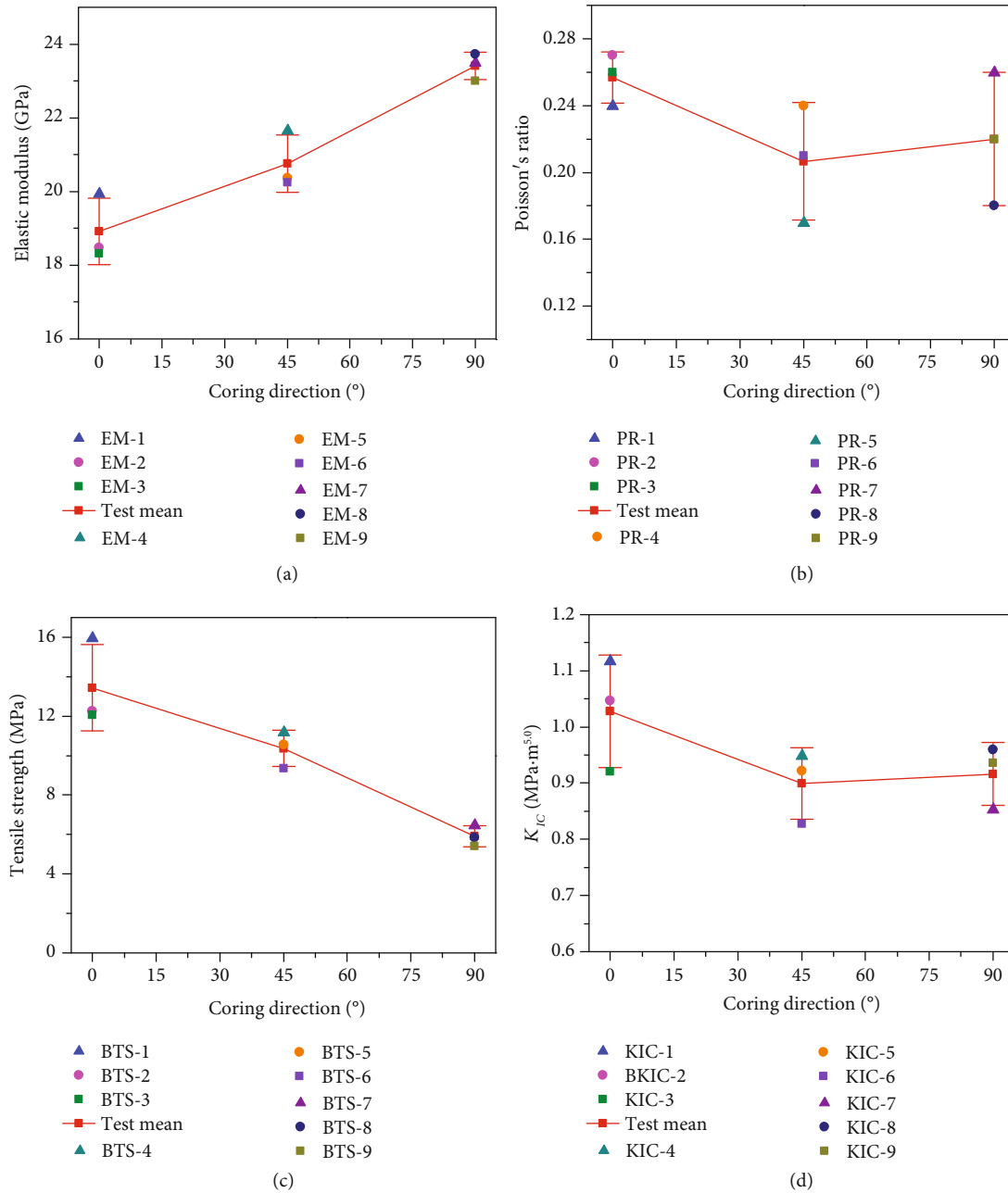


FIGURE 3: Anisotropic characteristics of shale rock. Here, EM denotes the elastic modulus, PR denotes Poisson’s ratio, BTS denotes the Brazilian tensile strength, and KIC denotes the fracture toughness: (a) anisotropic elastic modulus; (b) anisotropic Poisson’s ratio; (c) anisotropic tensile strength; (d) anisotropic fracture toughness.

0.122 mm for each of the tests. One thing to note is that the average fracture width generally displays a decreasing trend as the bedding dip angle increases, and the average fracture width that corresponds to $\beta = 0^\circ$ appears to be approximately four times that of $\beta = 90^\circ$. This implies that the anisotropic characteristics of shale rock have a remarkable impact on fracture width distribution. In addition, the fracture trajectory and fracture growth pattern also play certain role in fracture width evolution.

3.3. FIP Analysis: Theoretical vs. Experimental Results. As we all know, the FIP is mainly determined by analytical solu-

tions in actual engineering besides the usually adopted minifrac tests. Hence, it is extremely vitally significant for both drilling and hydraulic fracturing to analyze the adaptability of FIP models and improve their prediction accuracy by experimental methods. With this intent, several commonly used FIP models are reviewed, and the detailed background and derivation are given in Appendices A–C. To evaluate the precision of the predicted results of each model, the experimental FIP (EFIP) and theoretical FIP (TFIP) are drawn into a cross-plot, as displayed in Figure 5. The divergence indicator ($K = \text{TFIP}/\text{EFIP}$) is defined to characterize the degree of discrepancy. It can be noticed that the divergence indicator

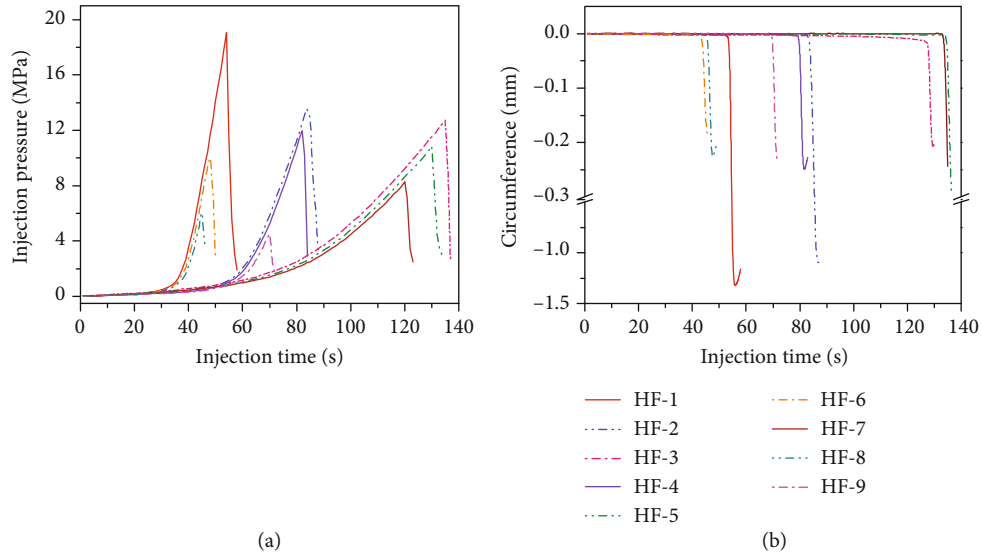


FIGURE 4: Measured injection pressure and radial displacement plotted with respect to injection time for various cases: (a) typical injection pressure curves; (b) evolution of radial deformation.

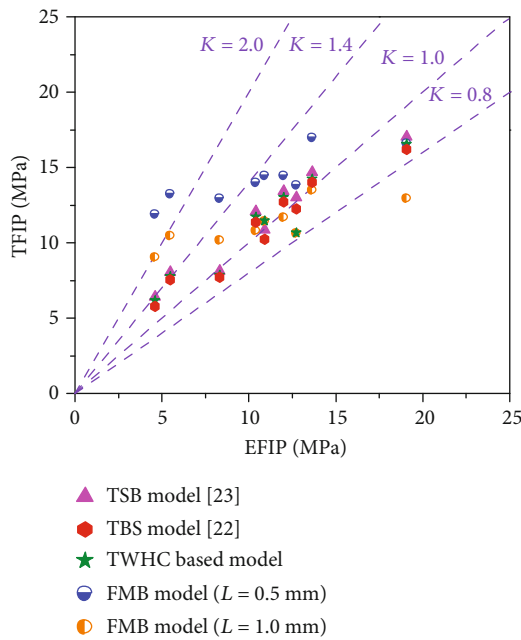


FIGURE 5: Cross-plot of TFIP vs. EFIP for the nine groups of fracturing tests.

belongs to 0.8 to 2.0 and most of them range between 0.8 and 1.4.

For the model derived from the anisotropic fracture toughness criterion, the predicted FIPs have a comparatively larger deviation from the experimental results, as shown in Figure 5. Though the prediction accuracy can be improved to some extent by increasing the preexisting fracture length moderately, the predictions have not shown the desired fluctuations with the bedding dip angle. The reason is that the stress intensity factor (SIF) model proposed by Rummel [36] is developed under the isotropic hypothesis. On the

other hand, the anisotropy of fracture toughness of Longmaxi shale is relatively weak such that the calculated FIP fluctuates slightly with the bedding dip angle. In terms of the other three models, such as the TWHC model, tensile strength anisotropy model [23], and full anisotropy model [22], they are established for intact borehole and rely on tensile strength to characterize the formation resistance to fracture initiation. Though a small discrepancy is observed between the predicted and the experiment results, the predicted FIP using the full anisotropy model may have a slight advantage over other models. In fact, the superiority of the full anisotropy model is not displayed very well, mainly because uniform horizontal stress is imposed on the specimen and it is almost negligible. Conversely, if there is a significant difference in horizontal stress, both the modulus and strength anisotropy should be accounted for in the prediction of FIP [22].

3.4. Factors Influencing FIP

3.4.1. Significance Analysis. According to the results shown in Figure 4, it is found that the bedding dip angle, borehole size, and injection rate have different levels of effects on the FIP. However, the significance of the effects of each factor on the FIP cannot be estimated directly from the acquirable information, which must be recurred to mathematics methods, such as variance analysis, to examine. The multiway analysis of variance (ANOVA) is performed using *anovan* function in MATLAB, and the specific calculation method has been described by Metcalfe et al. [37]. Generally, a larger significant difference means larger *F*-statistic and lower *P* value. It should be noted that the interactive effects of various factors are not taken into account here. As illustrated in Table 2, we can note that the bedding dip angle has the most significant impact on the FIP, next is borehole size, and the injection rate has the least effect. Meanwhile, we perform statistical analysis on the 9 groups of experiment

TABLE 2: ANOVA table.

Source of variation	Sums of squares (SS)	Degrees of freedom (df)	Mean squares (MS)	F-statistic	P value
Bedding dip angle	115.92	2	57.9601	50.22	0.0195
Borehole size	25.379	2	12.6893	10.99	0.0834
Injection rate	4.552	2	2.2762	1.97	0.3364
Error	2.308	2	1.54		
Total	148.159	8			

data, in hopes of gaining the effecting rules of each factor. The specific analysis process is described in the following subsection.

3.4.2. Effect of Borehole Size on EFIP. Figure 6 displays the effect of borehole size on the EFIPs of shale specimens with bedding dip angle $\beta = 0^\circ, 45^\circ,$ and 90° , where the last column represents the average EFIP at the given borehole size. It should be noted especially that the impact of the injection rate is ignored for the time being. We can clearly see that the EFIP of the shale specimen decreases with the increase of borehole size no matter what bedding dip angle is. For shale specimens with $\beta = 0^\circ$, the EFIPs are 19.06 MPa, 13.64 MPa, and 12.72 MPa for $R_w = 4$ mm, 5 mm, and 6 mm, respectively. The maximum reduction ratio is about 33.26%. Analogously, the biggest drop reaches 15.77% and 44.82% for $\beta = 45^\circ$ and $\beta = 90^\circ$, respectively. Besides, the average EFIP of each borehole size also shows significantly lower trends with the increase of R_w , and the maximum reduction ratio is 30.35%. This experimental conclusion has somewhat consistency with the numerical findings of Lecampion [38], though it is performed for homogeneous materials. In particular, Lecampion [38] sheds new light on the mechanism of fracture initiation from a wellbore and indicates that the size effect on FIP is controlled by a dimensionless parameter \mathfrak{R} ($\mathfrak{R} = K_{IC}^2/R_w T^2(\beta)$). By definition, the tensile fracture initiation from a wellbore is dominated by strength when $\mathfrak{R} < 0.1$, while it is governed by fracture energy when $\mathfrak{R} > 10$.

According to the parameters displayed in Figure 3, we can find that the calculated \mathfrak{R} 's are always in the intermediate situation, i.e., $1.22 < \mathfrak{R} < 5.41$. At this point, the tensile failure of the wellbore is governed by strength as well as fracture energy. Hence, some certain errors exist if we rely only on the tensile strength criterion, as shown in Figure 5. Of course, experimental error would also be the possible factor contributing to the deviation between theoretical analysis and experimental results.

3.4.3. Effect of Bedding Dip Angle on EFIP. Figure 7 illustrates the variation of EFIP with different bedding dip angles for the borehole radius of 4 mm, 5 mm, and 6 mm, where the last column represents the average EFIP for each bedding dip angle. Likewise, the influence of the injection rate is neglected due to its insignificant features. The result indicates that EFIP has a tendency of obvious dropping with the increase of the bedding dip angle. Take the shale samples of $R_w = 4$ mm as an example, the EFIPs are 19.06 MPa, 11.98 MPa, and 8.30 MPa for $\beta = 0^\circ, \beta = 45^\circ,$ and $\beta = 90^\circ$,

respectively. The biggest drop has reached 56.45%. Analogously, the biggest drop reaches 54.69% and 63.99% for $R_w = 5$ mm and $R_w = 6$ mm, respectively. Compared with borehole size, increasing the bedding dip angle can result in a much more significant decrease in EFIP. Besides, the average EFIP of each bedding dip angle also exhibits decreasing trend, and the maximum reduction ratio is 42.32%. The main reason for the occurrence of this phenomenon is that the tensile strength declines with the increase of the bedding dip angle. This implies that accurately testing tensile strength and selecting appropriate strength criteria are the most important aspects for the prediction of FIP during drilling and completion.

3.4.4. Effect of Injection Rate on EFIP. Figure 8 shows the EFIP with respect to various bedding dip angles under the injection rate of 0.15 mL/s, 0.35 mL/s, and 0.75 mL/s, in which the last column represents the average EFIP at a given injection rate. According to multivariate analysis, here, the size effect is ignored to discuss the interplay between injection rate and bedding dip angle. It is not difficult to see that the EFIP has no obvious variety regulation following the increase of the injection rate. The causes of this phenomenon may be an integrated result of various actions. On the one hand, the influence of borehole size on EFIP is greater than that of the injection rate. More importantly, there exists a threshold for the injection rate [32], which decides the actual fracture initiation behavior, but this critical value is still unknown. Actually, due to the sample differences and the heterogeneity of rock material, the relationship between injection rate and FIP has not been clearly understood so far through experiments. Experimental findings presented by Lin et al. [15] and Ranjith et al. [39] show that the EFIP increases accordingly with the injection rate, while Al-Nakhli et al. [40] point to the opposite conclusion. There are even those who claim that the injection rate affects EFIP depending on the permeability of rock [41, 42]. This does not, however, mean that the injection rate makes no difference to EFIP. It remains to be seen in further experiments.

4. Postfracturing Analysis

4.1. Macroscopic Fracture Morphology. The wellbore fracture-initiation patterns are vitally important to the design and operation of drilling and completion. For drilling engineering, rational and timely plugging the induced HFIs around the wellbore can effectively prevent and control the occurrence of lost circulation. For hydraulic fracturing

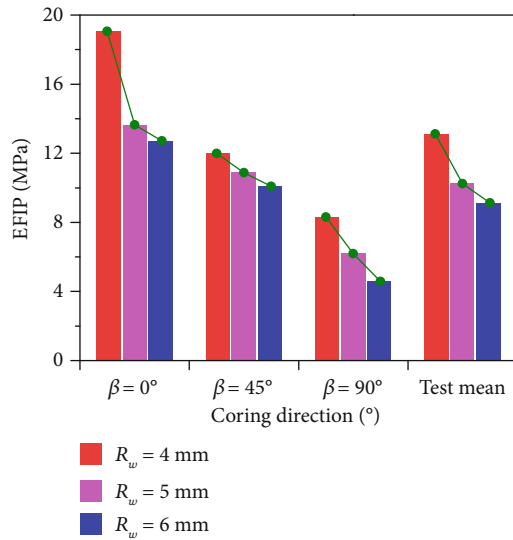


FIGURE 6: Influence of borehole size on FIP with bedding dip angle $\beta = 0^\circ$, 45° , and 90° .

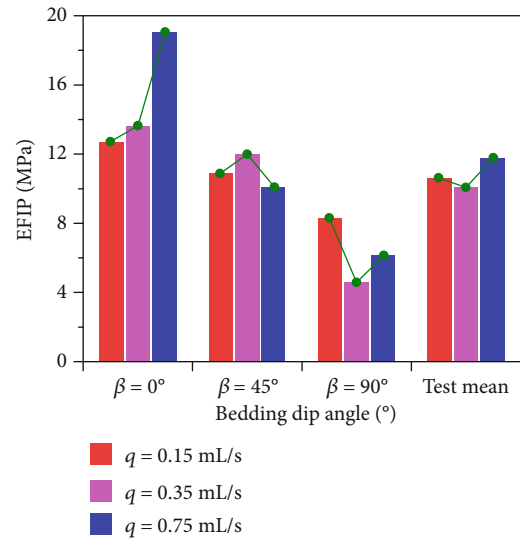


FIGURE 8: Influence of injection rate on FIP with bedding dip angle $\beta = 0^\circ$, 45° , and 90° .

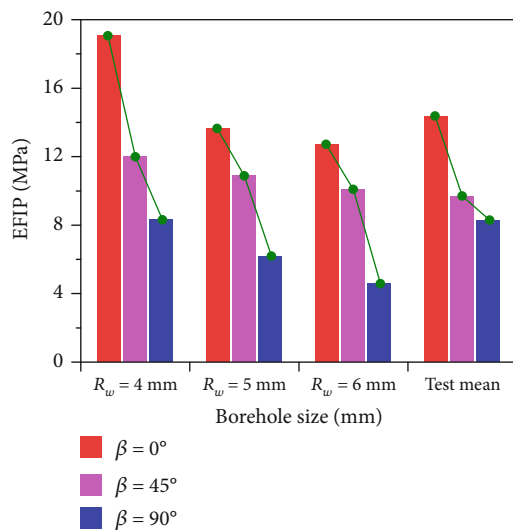


FIGURE 7: Influence of bedding dip angle on FIP with borehole size $R_w = 4$ mm, 5 mm, and 6 mm.

treatments, the formation of field-scale FNs is a progressive growth process from local to full domain, where the fracture initiation path under the core-plunger scale plays a decisive role. On account of this, the macroscopic morphology of HF's near-wellbore and its interaction with bedding planes are discussed. Figure 9 displays the ultimate macroscopic fracture morphology created by injection fluid, where the green lines denote the bedding planes and the red-dashed lines denote the fracture traces. The cleaved fracture planes are represented by capital letters, such as $ABCD$ and $A'B'C'D'$. Here, it needs to mention that the size of the triaxial pressure chamber of the experimental devices limits the dimension of the shale sample so that the initiated HF's

can propagate rapidly to its outside surface. In this case, the interplay between initiated fractures and bedding planes is impaired to some extent, but we can still capture several meaningful outcomes.

From Figure 9, we can clearly observe that the induced HF's mostly focus on one side rather than a symmetric distribution with regard to the wellbore, and the fracture initiation direction is not completely perpendicular to the borehole wall. The primary causes of these phenomena are that the shale specimen has obvious characteristics of heterogeneousness and anisotropy, and the borehole may not be exactly in the center of the specimen. More specifically, Figures 9(a)–9(c) display the macroscopic fracture morphology of samples at $\beta = 0^\circ$, where the fracture surfaces are nearly perpendicular to the bedding planes. It should be mentioned again that the axial stress is loaded to 25.0 MPa and the confining pressure is set as 0 MPa in the process of the experiment. The higher axial stress inhibits the opening of bedding planes to a certain extent. Even so, Figure 9(b) shows that the crack arrest occurs when the propagated HF's intersect with the bedding plane, and ultimately, the induced fractures grow thoroughly along the bedding planes; Figures 9(d)–9(f) show the macroscopic fracture morphology of samples at $\beta = 45^\circ$. We find that the HF's always grow along mechanically favorable directions, i.e., the HF's initially emanate from the borehole wall and then extend to a plane that is stressed relatively small. Even in this situation, some cases also present a weaker trend of growth along the bedding planes. The most probable cause of this phenomenon is the impact of axial stress, and on the other hand, the bedding planes have high consolidation strength. The previous study has also proved this viewpoint, where the HF's prefer to extend along the inclined bedding planes under the combined action of axial pressure and confining pressure [15]; Figures 9(h)–9(j) show the macroscopic fracture morphology of samples at $\beta = 90^\circ$, where the fracture surfaces are



FIGURE 9: Macroscopic fracture morphology of HF created on the shale specimens.

basically parallel with the bedding planes. The differences are that the initiation direction of specimens shown in Figure 9(h) intersects at a certain angle with the bedding plane and then deflects rapidly to the direction of the bedding plane, while Figure 9(i) shows the right-wing HF that initiates from the borehole and is arrested by a weak plane. These results indicate that bedding planes have great influences on FN formation. And predictably, the effects of rock anisotropy and bedding planes will be more apparent under the actual subsurface environment.

4.2. Microscopic Fracture Morphology. The microtopography of crack mainly refers to the fluctuation of the fracture surface created after the fracturing experiment. Using a 3D laser scanner, the point cloud data of the real fracture surfaces is acquired, and then, the 3D models of fracture surfaces can be reconstructed, as depicted in Figure 10.

According to the complementary relationship between fracture surfaces, Figure 10 just provides the processing results on one side. We can clearly observe that hydraulic fracturing results in an uneven finish with peaks and valleys in the depth of the fracture surface. Meanwhile, the geometric size and distribution density of asperities on the fracture surface are physically different from each other. This illustrates that the contact problem on the fracture surfaces becomes more complex under the impact of rock heteroge-

neity, anisotropy, and weak structural plane. On the other hand, the fracture surfaces of part of the samples are relatively smooth or grainy, as shown in Figures 10(b), 10(d), and 10(i). In addition, it is important to emphasize that the excessive rugged fracture surfaces will not only increase the frictional pressure of fluid flow but also bring difficulties for the migration and placement of proppant.

5. Conclusions

- (1) Anisotropy properties of Longmaxi formation shale, including elastic modulus, Poisson's ratio, tensile strength, and fracture toughness, are thoroughly investigated based on fundamental rock mechanics experiments. Results show that shale rock exhibits strong elastic and strength anisotropy. The elastic modulus appears a significant upward trend with the increase of the bedding dip angle, while the tensile strength shows an opposite character. The anisotropies of Poisson's ratio and fracture toughness in different bedding dip angles are comparatively weak.
- (2) The hydraulic fracturing experiments under the core-plunger scale show that the bedding dip angle reflected by rock anisotropy has the most significant

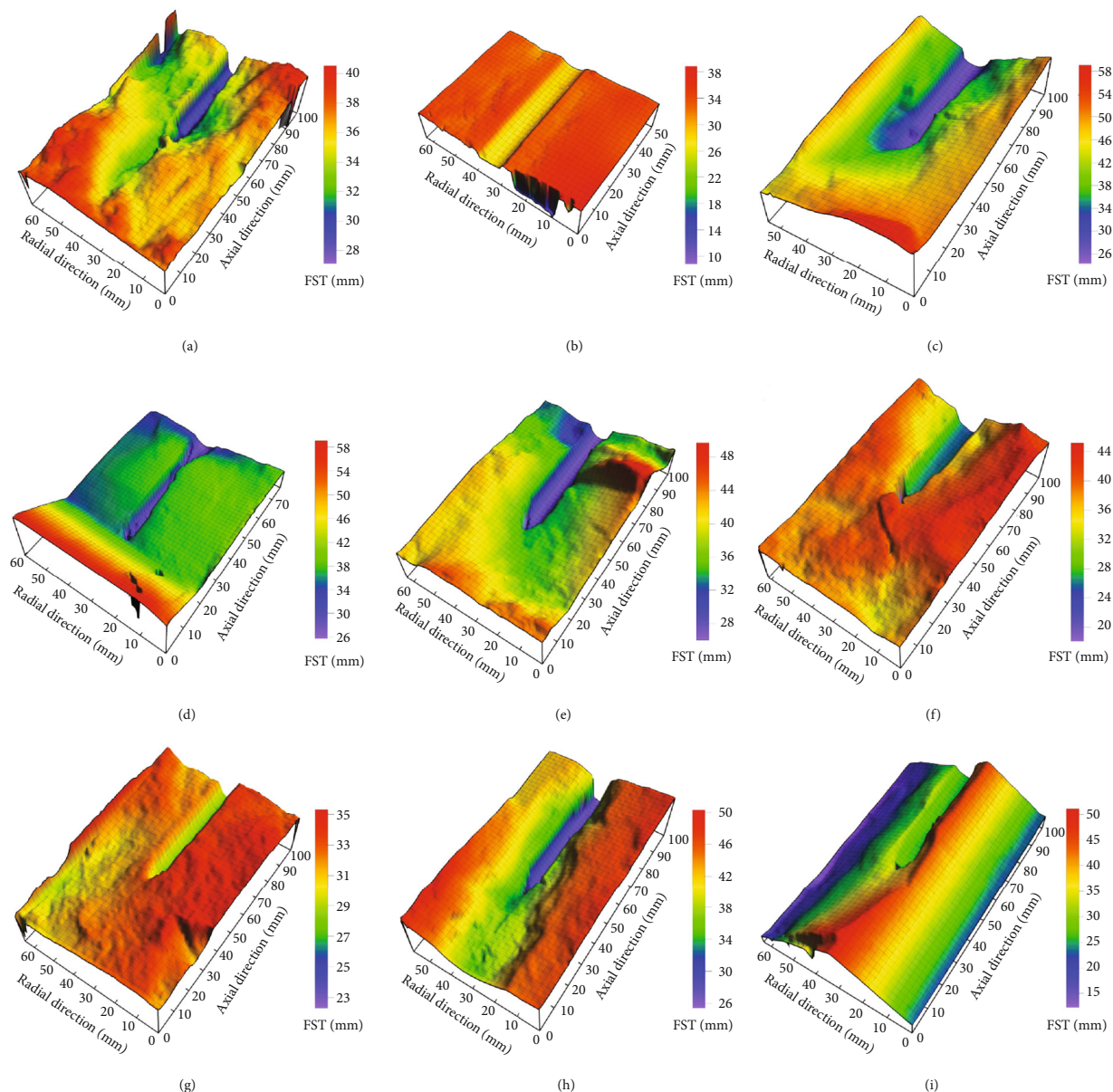


FIGURE 10: 3D morphological map of fracture surface for different specimens; here, FST represents the fracture surface topography.

impact on the EFIP, next is borehole size, and injection rate has the least effect. The EFIP of the shale specimen decreases as the borehole size and bedding dip angle increase. It is also found that the increase of the bedding dip angle may result in a decline of the equivalent fracture opening. According to a dimensionless parameter defined by Lecampion [38], we infer that the mechanism of crack initiation from a wellbore is governed by strength as well as fracture energy, but strength-driven is prevailing

- (3) The data of EFIP is adopted for examining the adaptability of several commonly used FIP models in laminated shale formations. The results of the full anisotropy model have a certain advantage compared with the TWHC model, TBS model, and

FMB model. This illustrates that it is necessary to take into account both anisotropic modulus and tensile strength during predicting the FIP of shale formations. The FMB model may take effect for formation with strong fracture toughness anisotropy, but it remains to be confirmed

- (4) Postfracturing analysis displays that the macroscopic fracture morphologies mostly focus on one side rather than a symmetric distribution with regard to the wellbore, and the fracture initiation direction is not completely perpendicular to the borehole wall. Three different interaction scenarios are observed when the initiated HF encounters the weak bedding plane. Microscopic scanning shows that hydraulic fracturing results in an uneven finish with peaks

and valleys in the depth of the fracture surface. The geometric size and distribution density of asperities on the fracture surface are physically different from each other

Appendix

A. FIP Estimate for Formations with Anisotropic Rock Strengths

The physical model for the fracturing experiment of the specimen, as illustrated in Figure 1(d), can be constructed in terms of thick-walled hollow cylinder (TWHC) theory if the material anisotropy is not considered. The radial (σ_r) and hoop (σ_θ) stress components acting on the borehole wall in polar coordinates satisfy the plane-strain equilibrium equation ([43]):

$$\frac{d\sigma_r}{dr} + \frac{\sigma_r - \sigma_\theta}{r} = 0. \quad (\text{A.1})$$

In addition, the compatibility equation is given by

$$\frac{d\sigma_\theta}{dr} - \nu \frac{d\sigma_r}{dr} = \frac{1 + \nu}{r} (\sigma_r - \sigma_\theta). \quad (\text{A.2})$$

Consider a hollow cylinder defined by $R_w < r < R$, the boundary conditions at the inner and outer wall surfaces satisfy

$$\begin{aligned} \sigma_r(R_w) &= P_w, \\ \sigma_r(R) &= P_0, \end{aligned} \quad (\text{A.3})$$

where P_0 is the confining pressure, P_w is the wellbore pressure, R_w is the radius of hole, and R is the diameter of the cylinder.

Substituting Equation (A.1) into Equation (A.2) and imposing the boundary condition Equation (A.3), the tangential stress around the borehole wall can be expressed as

$$\sigma_\theta = \frac{(R^2 P_0 - R_w^2 P_w)}{(R^2 - R_w^2)} - \frac{R_w^2 R^2 (P_w - P_0)}{(R^2 - R_w^2) r^2}. \quad (\text{A.4})$$

Ma et al. [23] compare four typical anisotropic tensile failure criteria based on the laboratory data and indicate that the Novae-Zaninetti (N-Z) criterion can describe the ATS of shale rock more accurately. Hence, the N-Z criterion is employed to predict the FIP of shale rock, which is expressed as [44]

$$T(\beta_b) = \frac{T_m T_b}{T_b \sin^2 \beta_b + T_m \cos^2 \beta_b}, \quad (\text{A.5})$$

where $T(\beta_b)$ is the anisotropic tensile strength at a given angle β_b , β_b is the angle between the tensile stress and bedding normal, T_b is the tensile strength of bedding planes, and T_m is the tensile strength of the rock matrix.

Wellbore tensile failure occurs when the tangential stress around the borehole wall exceeds the tensile strength $T(\beta_b)$. Namely [45],

$$\sigma_\theta|_{r=R_w} + T(\beta_b) = 0. \quad (\text{A.6})$$

Substituting Equations (A.4) and (A.5) into Equation (A.6) and solving for the wellbore pressure, it leads to

$$P_{\text{FIP}} = \frac{2R^2 P_0 + T(\beta_b)(R^2 - R_w^2)}{R_w^2 + R^2}. \quad (\text{A.7})$$

B. FIP Estimate for Transversely Isotropic Formations

For vertical wells in transversely isotropic formations, the closed-form solution of stress distribution around the wellbore is given by Amadei [46]. It is regarded as a superposition of far-field stresses and the induced stresses by excavation and wellbore pressure. Namely,

$$\begin{cases} \sigma_x = \sigma_{x,0} + \sigma_{x,i} + \sigma_{x,b}, \\ \sigma_y = \sigma_{y,0} + \sigma_{y,i} + \sigma_{y,b}, \\ \tau_{xy} = \tau_{xy,0} + \tau_{xy,i} + \tau_{xy,b}, \\ \tau_{xz} = \tau_{xz,0} + \tau_{xz,i} + \tau_{xz,b}, \\ \tau_{yz} = \tau_{yz,0} + \tau_{yz,i} + \tau_{yz,b}, \\ \sigma_z = \sigma_{z,0} + \sigma_{z,i} + \sigma_{z,b}, \end{cases} \quad (\text{B.1})$$

where $\sigma_{x,0}$, $\sigma_{y,0}$, $\sigma_{z,0}$, $\tau_{xy,0}$, $\tau_{yz,0}$, and $\tau_{xz,0}$, respectively, represent the far-field stress components; $\sigma_{x,i}$, $\sigma_{y,i}$, $\sigma_{z,i}$, $\tau_{xy,i}$, $\tau_{yz,i}$, and $\tau_{xz,i}$, respectively, represent the stress components induced by excavation; and $\sigma_{x,b}$, $\sigma_{y,b}$, $\sigma_{z,b}$, $\tau_{xy,b}$, $\tau_{yz,b}$, and $\tau_{xz,b}$, respectively, represent the stress components induced by wellbore pressure. The detailed expressions of these stress components are defined in Ma et al. [22].

Since the above stress tensor is presented for the borehole Cartesian coordinate system, it needs to be transformed into the borehole cylindrical coordinate system before calculating the stress distributions. According to transformation formulas, the general solutions for the stress distributions around the borehole wall can be written as [47]

$$\begin{cases} \sigma_r = P_w, \\ \sigma_\theta = \sigma_x \sin^2 \theta + \sigma_y \cos^2 \theta - \tau_{xy} \sin 2\theta, \\ \sigma_z = \sigma_z, \\ \tau_{r\theta} = -0.5\sigma_x \sin 2\theta + 0.5\sigma_y \sin 2\theta + \tau_{xy} \cos 2\theta, \\ \tau_{\theta z} = \tau_{yz} \cos \theta - \tau_{xz} \sin \theta, \\ \tau_{rz} = \tau_{yz} \sin \theta + \tau_{xz} \cos \theta. \end{cases} \quad (\text{B.2})$$

Substituting Equation (B.2) into Equation (A.6), the critical wellbore pressure that satisfies the wellbore tensile failure condition can be expressed as

$$P_{\text{FIP}} = \min \{P_{wc}(\theta)\} = \frac{T(\beta_b) + A\sigma_h + B\sigma_H}{C}, \quad (\text{B.3})$$

where the coefficients of A , B , and C in Equation (B.3) have been given by Ma et al. [22], and here, we will not repeat the detailed derivation process; σ_H is the maximum horizontal far-field stress; σ_h is the minimum horizontal far-field stress.

Particularly, if the effect of the anisotropic modulus is ignored, the FIP for a vertical well can be calculated by the following simplified model ([23]):

$$P_{\text{FIP}} = 3\sigma_h - \sigma_H + T(\beta_b). \quad (\text{B.4})$$

C. FIP Estimate for Formations with Anisotropic Fracture Toughness

To analyze the problem of preexisting biwing fracture emanating from a wellbore, Rummel [36] derived a closed-form solution for the stress intensity factors (SIFs) at the crack tip, which were induced by in situ stress (σ_H, σ_h), wellbore pressure (P_w), and fracture internal pressure (P_f) and can be formulated as

$$\begin{aligned} K_I(\sigma_H, \sigma_h, P_w, P_f) &= K_I(\sigma_H) + K_I(\sigma_h) + K_I(P_w) + K_I(P_f) \\ &= -\sigma_H \sqrt{R_w} f(b) - \sigma_h \sqrt{R_w} g(b) \\ &\quad + P_w \sqrt{R_w} h_0(b) + P_f \sqrt{R_w} h_a(b), \end{aligned} \quad (\text{C.1})$$

where K_I is the total SIF for mode I fracture growth, b is the dimensionless length parameter and $b = 1 + L/R_w$, and L is the length of preexisting fracture. $f(b)$, $g(b)$, $h_0(b)$, and $h_a(b)$ are dimensionless SIF created by σ_H , σ_h , P_w , and P_f , respectively, which are defined as follows:

$$f(b) = -2 \left[\frac{b^2 - 1}{\pi b^7} \right]^{1/2}, \quad (\text{C.2})$$

$$g(b) = (\pi b)^{1/2} \left(1 - \frac{2}{\pi} \sin^{-1} \frac{1}{b} \right) + 2(b^2 + 1) \left[\frac{b^2 - 1}{\pi b^7} \right]^{1/2}, \quad (\text{C.3})$$

$$h_0(b) = \frac{1.3(b-1)}{1+b^{1.5}} + 7.8 \frac{\sin[(b-1)/2]}{2b^{2.5}-1.7}, \quad (\text{C.4})$$

$$h_a(b) = \lambda(\pi b)^{1/2} \left(1 - \frac{2}{\pi} \sin^{-1} \frac{1}{b} \right), \quad (\text{C.5})$$

where λ denotes the degree of fluid invasion and $\lambda = 0$ represents the preexisting fractures which are uninvaded and $P_f = 0$, while $\lambda = 1$ means the preexisting fractures are fully invaded and $P_f = P_w$.

For laminated materials, the variation of fracture toughness usually displays directional dependence, which can be written as [48]

$$K_{IC}(\beta_0) = K_{IC,1} \cos^2 \beta_0 + K_{IC,2} \sin^2 \beta_0, \quad (\text{C.6})$$

where $K_{IC,1}$ and $K_{IC,2}$, respectively, represent the critical SIF at $\beta_0 = 0^\circ$ and $\beta_0 = 90^\circ$ and β_0 represents the angle between the direction of preexisting fracture and bedding plane.

Fracture initiation occurs once the SIF at the fracture tip reaches the fracture toughness of the formation rock [$K_I = K_{IC}(\beta_0)$]. Therefore, the FIP for laminated formations with anisotropic fracture toughness can be determined by

$$P_{\text{FIP}} = \frac{1}{h_0(b) + h_a(b)} + \left[\frac{K_{IC}(\beta_0)}{\sqrt{R_w}} + \sigma_H f(b) + \sigma_h g(b) \right]. \quad (\text{C.7})$$

Data Availability

All data used during the study are available from the corresponding author by request.

Conflicts of Interest

The authors declare that they have no conflicts of interest.

Acknowledgments

This work was supported by the Sichuan Science and Technology Program (Grant Nos. 2021YFH0047 and 2020JDJQ0055), the Fok Ying Tong Education Foundation, China (Grant No. 171097), the Youth Scientific and Technological Innovation Team Foundation of Southwest Petroleum University (Grant No. 2019CXTD09), and the Program of Introducing Talents of Discipline to Chinese Universities (111 Plan) (Grant No. D18016).

References

- [1] E. Hoek and C. D. Martin, "Fracture initiation and propagation in intact rock - A review," *Journal of Rock Mechanics and Geotechnical Engineering*, vol. 6, no. 4, pp. 287–300, 2014.
- [2] B. C. Haimson and F. H. Cornet, "ISRM Suggested Methods for rock stress estimation-Part 3: hydraulic fracturing (HF) and/or hydraulic testing of pre-existing fractures (HTPF)," *International Journal of Rock Mechanics and Mining Sciences*, vol. 40, no. 7-8, pp. 1011–1020, 2003.
- [3] Z. Sun, J. Shi, K. Wu, T. Zhang, D. Feng, and X. Li, "Effect of pressure-propagation behavior on production performance: implication for advancing low-permeability coalbed-methane recovery," *SPE Journal*, vol. 24, no. 2, pp. 681–697, 2019.
- [4] A. P. Bungler and G. Y. Lu, "Time-dependent initiation of multiple hydraulic fractures in a formation with varying stresses and strength," *SPE Journal*, vol. 20, no. 6, pp. 1317–1325, 2015.
- [5] J. F. W. Gale, R. M. Reed, and J. Holder, "Natural fractures in the Barnett shale and their importance for hydraulic fracture treatments," *AAPG Bulletin*, vol. 91, no. 4, pp. 603–622, 2007.

- [6] L. J. L. Beugelsdijk, C. J. De Pater, and K. Sato, "Experimental hydraulic fracture propagation in a multi-fractured medium," in *SPE Asia Pacific Conference on Integrated Modelling for Asset Management*, Yokohama, Japan, 2000.
- [7] J. Zhou and C. J. Xue, "Experimental investigation of fracture interaction between natural fractures and hydraulic fracture in naturally fractured reservoirs," in *SPE Europec/Eage Annual Conference and Exhibition*, Vienna, Austria, 2011.
- [8] H. Abass and C. Lamei, *Hydraulic fracturing: experimental modeling. Hydraulic Fracture Modeling*, Gulf Professional Publishing, 2018.
- [9] J. Zhou, M. Chen, Y. Jin, and G. Q. Zhang, "Analysis of fracture propagation behavior and fracture geometry using a tri-axial fracturing system in naturally fractured reservoirs," *International Journal of Rock Mechanics and Mining Sciences*, vol. 45, no. 7, pp. 1143–1152, 2008.
- [10] H. Gu, X. Weng, J. B. Lund, M. G. Mack, U. Ganguly, and R. Suarez-Rivera, "Hydraulic fracture crossing natural fracture at nonorthogonal angles: a criterion and its validation," *SPE Production & Operations*, vol. 27, no. 1, pp. 20–26, 2012.
- [11] D. Chuprakov, O. Melchaeva, and R. Prioul, "Injection-sensitive mechanics of hydraulic fracture interaction with discontinuities," *Rock Mechanics and Rock Engineering*, vol. 47, no. 5, pp. 1625–1640, 2014.
- [12] A. S. Athavale and J. L. Miskimins, "Laboratory Hydraulic Fracturing Tests on Small Homogeneous and Laminated Blocks," in *The 42nd U.S. Rock Mechanics Symposium*, ARMA, San Francisco, California, 2008.
- [13] J. E. Olson, B. Bahorich, and J. Holder, "Examining hydraulic fracture: natural fracture interaction in hydrostone block experiments," in *SPE Hydraulic Fracturing Technology Conference*, The Woodlands, Texas, 2012.
- [14] T. G. Fan and G. Q. Zhang, "Laboratory investigation of hydraulic fracture networks in formations with continuous orthogonal fractures," *Energy*, vol. 74, pp. 164–173, 2014.
- [15] C. Lin, J. He, X. Li, X. Wan, and B. Zheng, "An experimental investigation into the effects of the anisotropy of shale on hydraulic fracture propagation," *Rock Mechanics and Rock Engineering*, vol. 50, no. 3, pp. 543–554, 2017.
- [16] Z. Bennour, T. Ishida, Y. Nagaya et al., "Crack extension in hydraulic fracturing of shale cores using viscous oil, water, and liquid carbon dioxide," *Rock Mechanics and Rock Engineering*, vol. 48, no. 4, pp. 1463–1473, 2015.
- [17] T. Guo, S. Zhang, Z. Qu, T. Zhou, Y. Xiao, and J. Gao, "Experimental study of hydraulic fracturing for shale by stimulated reservoir volume," *Fuel*, vol. 128, pp. 373–380, 2014.
- [18] N. Li, S. Zhang, Y. Zou et al., "Acoustic emission response of laboratory hydraulic fracturing in layered shale," *Rock Mechanics and Rock Engineering*, vol. 51, no. 11, pp. 3395–3406, 2018.
- [19] M. R. Chandler, P. G. Meredith, N. Brantut, and B. R. Crawford, "Fracture toughness anisotropy in shale," *Journal of Geophysical Research: Solid Earth*, vol. 121, no. 3, pp. 1706–1729, 2016.
- [20] Y. Liu, T. Ma, H. Wu, and P. Chen, "Investigation on mechanical behaviors of shale cap rock for geological energy storage by linking macroscopic to mesoscopic failures," *Journal of Energy Storage*, vol. 29, article 101326, 2020.
- [21] C. M. Sayers, "The effect of anisotropy on the Young's moduli and Poisson's ratios of shales," *Geophysical Prospecting*, vol. 61, no. 2, pp. 416–426, 2013.
- [22] T. S. Ma, Y. Liu, P. Chen, B. S. Wu, J. H. Fu, and Z. X. Guo, "Fracture-initiation pressure prediction for transversely isotropic formations," *Journal of Petroleum Science and Engineering*, vol. 176, pp. 821–835, 2019.
- [23] T. S. Ma, Q. B. Zhang, P. Chen, C. H. Yang, and J. Zhao, "Fracture pressure model for inclined wells in layered formations with anisotropic rock strengths," *Journal of Petroleum Science and Engineering*, vol. 149, pp. 393–408, 2017.
- [24] Y. J. Zeng, X. C. Jin, S. D. Ding et al., "Breakdown pressure prediction with weight function method and experimental verification," *Engineering Fracture Mechanics*, vol. 214, pp. 62–78, 2019.
- [25] X. Zhang, R. G. Jeffrey, and M. Thiercelin, "Deflection and propagation of fluid-driven fractures at frictional bedding interfaces: a numerical investigation," *Journal of Structural Geology*, vol. 29, no. 3, pp. 396–410, 2007.
- [26] X. Zhang, R. G. Jeffrey, A. P. Bunger, and M. Thiercelin, "Initiation and growth of a hydraulic fracture from a circular wellbore," *International Journal of Rock Mechanics and Mining Sciences*, vol. 48, no. 6, pp. 984–995, 2011.
- [27] B. Lecampion, J. Desroches, R. G. Jeffrey, and A. P. Bunger, "Experiments versus theory for the initiation and propagation of radial hydraulic fractures in low-permeability materials," *Journal of Geophysical Research: Solid Earth*, vol. 122, no. 2, pp. 1239–1263, 2017.
- [28] Z. Chen, R. G. Jeffrey, X. Zhang, and J. Kear, "Finite-element simulation of a hydraulic fracture interacting with a natural fracture," *SPE Journal*, vol. 22, no. 1, pp. 219–234, 2017.
- [29] Y. Liu, P. Chen, B. Wu et al., "Mechanics of hydraulic-fracture growth from a wellbore intersecting natural fractures," *SPE Journal*, vol. 25, no. 2, pp. 646–661, 2020.
- [30] Y. Feng, G. Li, Y. Meng, and B. Guo, "A novel approach to investigating transport of lost circulation materials in rough fracture," *Energies*, vol. 11, no. 10, p. 2572, 2018.
- [31] R. Sahai and R. G. Moghanloo, "Proppant transport in complex fracture networks - A review," *Journal of Petroleum Science and Engineering*, vol. 182, p. 106199, 2019.
- [32] L. Zhuang, K. Y. Kim, S. G. Jung, M. Diaz, and K. B. Min, "Effect of water infiltration, injection rate and anisotropy on hydraulic fracturing behavior of granite," *Rock Mechanics and Rock Engineering*, vol. 52, no. 2, pp. 575–589, 2019.
- [33] W. A. M. Wanniarachchi, R. P. Gamage, M. S. A. Perera, T. D. Rathnaweera, M. Gao, and E. Padmanabhan, "Investigation of depth and injection pressure effects on breakdown pressure and fracture permeability of shale reservoirs: an experimental study," *Applied Sciences*, vol. 7, no. 7, p. 664, 2017.
- [34] Z. Jin, W. Li, C. Jin, J. Hambleton, and G. Cusatis, "Anisotropic elastic, strength, and fracture properties of Marcellus shale," *International Journal of Rock Mechanics and Mining Sciences*, vol. 109, pp. 124–137, 2018.
- [35] C. Lin, J. He, and X. Li, "Width evolution of the hydraulic fractures in different reservoir rocks," *Rock Mechanics and Rock Engineering*, vol. 51, no. 5, pp. 1621–1627, 2018.
- [36] F. Rummel, "Fracture mechanics approach to hydraulic fracturing stress measurements," in *Fracture Mechanics of Rock*, pp. 217–240, Elsevier, 1987.
- [37] A. Metcalfe, D. Green, T. Greenfield, M. Mansor, A. Smith, and J. Tuke, *Statistics in Engineering: with Examples in MATLAB and R*, Chapman and Hall/CRC, Boca Raton, FL, 2nd edition, 2019.

- [38] B. Lecampion, "Modeling size effects associated with tensile fracture initiation from a wellbore," *International Journal of Rock Mechanics and Mining Sciences*, vol. 56, pp. 67–76, 2012.
- [39] P. G. Ranjith, W. A. M. Wanniarachchi, M. S. A. Perera, and T. D. Rathnaweera, "Investigation of the effect of foam flow rate on foam-based hydraulic fracturing of shale reservoir rocks with natural fractures: an experimental study," *Journal of Petroleum Science and Engineering*, vol. 169, pp. 518–531, 2018.
- [40] A. Al-Nakhli, T. Zeeshan, M. Mahmoud, and A. Abdulaheem, "Reducing breakdown pressure of tight reservoirs via in-situ pulses: impact of mineralogy," in *SPE/IATMI Asia Pacific Oil & Gas Conference and Exhibition*, Bali, Indonesia, 2019.
- [41] E. Detournay and A. Cheng, "Influence of pressurization rate on the magnitude of the breakdown pressure," in *33th US Symposium on Rock Mechanics*, ARMA, 1992.
- [42] M. D. Zoback, F. Rummel, R. Jung, and C. B. Raleigh, "Laboratory hydraulic fracturing experiments in intact and pre-fractured rock," *International Journal of Rock Mechanics and Mining Sciences & Geomechanics Abstracts*, vol. 14, no. 2, pp. 49–58, 1977.
- [43] S. Timoshenko, *Strength of Materials, Part II: Advanced Theory and Problems*, D. van Nostrand Company, 3rd edition, 1963.
- [44] R. Nova and A. Zaninetti, "An investigation into the tensile behaviour of a schistose rock," *International Journal of Rock Mechanics and Mining Sciences & Geomechanics Abstracts*, vol. 27, no. 4, pp. 231–242, 1990.
- [45] W. B. Bradley, "Failure of inclined Boreholes," *Journal of Energy Resources Technology- Transactions of The ASME*, vol. 101, no. 4, pp. 232–239, 1979.
- [46] B. Amadei, *Rock Anisotropy and the Theory of Stress Measurements*, Springer Science & Business Media, 1983.
- [47] B. S. Aadnoy and M. E. Chenevert, "Stability of highly inclined boreholes (includes associated papers 18596 and 18736)," *SPE Drilling Engineering*, vol. 2, no. 4, pp. 364–374, 1987.
- [48] M. B. Buczek and C. T. Herakovich, "A normal stress criterion for crack extension direction in orthotropic composite materials," *Journal of Composite Materials*, vol. 19, no. 6, pp. 544–553, 1985.